



LAWRENCE
LIVERMORE
NATIONAL
LABORATORY

Performance of a MEMS-based AO-OCT system using Fourier Reconstruction

J. Evans, R. Zawadzki, S. Jones, S. Olivier, J. S
Werner

February 9, 2009

Photonics West
San Jose, CA, United States
January 24, 2009 through January 29, 2009

Disclaimer

This document was prepared as an account of work sponsored by an agency of the United States government. Neither the United States government nor Lawrence Livermore National Security, LLC, nor any of their employees makes any warranty, expressed or implied, or assumes any legal liability or responsibility for the accuracy, completeness, or usefulness of any information, apparatus, product, or process disclosed, or represents that its use would not infringe privately owned rights. Reference herein to any specific commercial product, process, or service by trade name, trademark, manufacturer, or otherwise does not necessarily constitute or imply its endorsement, recommendation, or favoring by the United States government or Lawrence Livermore National Security, LLC. The views and opinions of authors expressed herein do not necessarily state or reflect those of the United States government or Lawrence Livermore National Security, LLC, and shall not be used for advertising or product endorsement purposes.

Performance of a MEMS-based AO-OCT System using Fourier Reconstruction

Julia W. Evans^{a,b}, Robert J. Zawadzki^b, Steve Jones^a, Scot Olivier^a,
John S. Werner^b

^aLawrence Livermore National Laboratory
7000 East Avenue, Livermore 94550

^bVision Science and Advanced Retinal Imaging Laboratory, Department of Ophthalmology &
Vision Science, University of California, Davis,
Sacramento, CA 95817

ABSTRACT

Adaptive optics (AO) and optical coherence tomography (OCT) are powerful imaging modalities that, when combined, can provide high-resolution (3.5 μm isotropic), 3-D images of the retina. The AO-OCT system at UC Davis has demonstrated the utility of this technology for microscopic, volumetric, *in vivo* retinal imaging. The current system uses an AOptix bimorph deformable mirror (DM) for low-order, high-stroke correction and a 140-actuator Boston Micromachines DM for high-order correction. Developments to improve performance or functionality of the instrument are on-going. Based on previous work in system characterization we have focused on improved AO control. We present preliminary results and remaining challenges for a newly implemented Fourier transform reconstructor (FTR). The previously reported error budget analysis is also reviewed and updated, with consideration of how to improve both the amount of residual error and the robustness of the system. Careful characterization of the AO system will lead to improved performance and inform the design of future systems.

Keywords: Adaptive Optics, MEMS deformable mirror, optical coherence tomography

1. INTRODUCTION

The Adaptive optics (AO)-optical coherence tomography (OCT) system at UC Davis has been in use for several years and has demonstrated the utility of this technology for microscopic, volumetric, *in vivo* retinal imaging.¹ The combined technology of traditional OCT and adaptive optics provides excellent resolution in all three dimensions. We estimate that our AO-OCT has resolution of 3.5 μm isotropic.² Development of OCT is ongoing including new advanced light sources³ and the addition of SLO imaging modalities.⁴

We are also working to improve the AO subsystem and our efforts in this area are the focus of this proceeding. In this case we are not trying to improve the overall lateral resolution of the instrument through more advanced AO but to improve the contrast of the OCT images through improved AO correction. We are also interested in improving the robustness of the system with regard to the number of subjects that can be successfully imaged in the system. System characterization is critical for understanding and ultimately improving AO performance. An error budget is a common way to summarize the error sources of a system, but can give an incomplete picture of the overall performance of a system if variation in the size of errors (often caused by variation between subjects in vision science AO systems) is not taken into account.

In our previous work in this area we identified low-spatial frequency error as the largest source of error in the system. Here we summarize our characterization efforts, as assessing these errors is generally incremental and iterative, and we continue to explore the source of the previously identified low-order error. In particular, we present preliminary tests with a model eye of the Fourier Transform Reconstructor (FTR), which we hope will correct the low-order error observed with the previous control system. We summarize the error sources in an error budget and discuss the limitations of an error budget for understanding the robustness of system performance.

Send correspondence to evans74@llnl.gov

2. SYSTEM DESCRIPTION

An OCT system is basically an interferometer with a sample arm and a reference arm. The AO-OCT system is described in previous publications.³ The sample arm contains the AO subsystem and thus is the focus of this proceeding. It is shown in Fig. 1. The major components of the AO subsystem are the 20×20 Shack-Hartman wavefront sensor (WFS), and two deformable mirrors. Spherical mirrors (indicated by S1-S10 in the diagram) re-image the pupil. The system uses a bimorph deformable mirror (DM) made by AOptix Technologies, Inc. for low-order, high-stroke correction⁵ and a 140-actuator micro-electrical-mechanical-system (MEMS) DM made by Boston Micromachines Corporation (BMC) for high-order correction.⁶ These are indicated by DM1 and DM2 in the layout. Like several other imaging modalities, OCT requires the sample arm to scan the retina to produce the science image. Horizontal and vertical scanners are located at pupil planes and indicated by horiz. and vert. in the diagram. For some characterization tasks we use a model eye, consisting of a lens with a paper ‘retina’ at the focus.

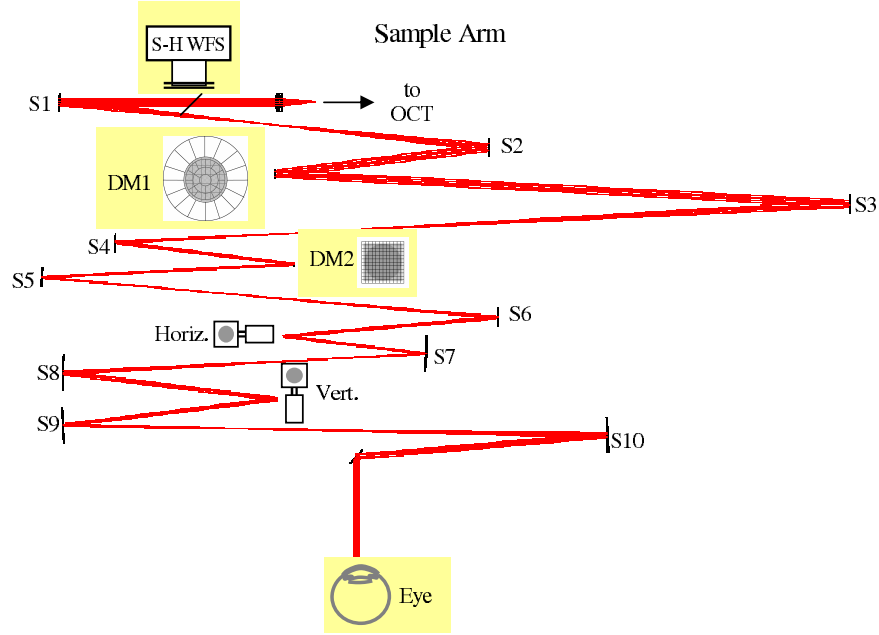


Figure 1. Layout of the AO-OCT sample arm. The system uses a 20×20 Shack-Hartmann wavefront sensor, a bimorph deformable mirror for low-order correction and a MEMS deformable mirror for high-order correction. Horizontal and vertical scanners are used to scan the retina. S1 - S10 denote spherical mirrors used to re-image the pupil plane. A sample arm like this could also be used for other imaging modalities, such as AO-SLO.

A description of the basic AO operation is available from several previous publications;^{3,7} it is summarized here for the convenience of the reader. Prior to closed-loop operation the position of the reference centroids and the control matrices for each DM are measured. The reference centroids are measured in ‘calibration’ mode; A flat mirror is placed in front of S1 and is adjusted to maximize back-coupled light to the input fiber, then the centroid positions are measured. The control matrices (one for each DM) are calculated from the system matrix found by actuating each actuator in the system in single-pass mode. In single-pass mode a fiber and collimating lens are placed in the eye position and adjusted to maximize the light coupled back to the input fiber used in double-pass operation. Typically the bimorph is measured first, then held flat while the MEMS is measured. During closed-loop operation the calculated control matrices are used to close the loop on the two DMs consecutively.³ The double-DM configuration is also described for an AO-SLO system in Chen et al.⁸ During closed-loop operation the rms of centroid displacements is used to gauge performance. During post-processing the FTR is used to examine residual WFE.⁹

The real-time controller is written in C with GUI interface written in Java. It has the advantage of being robust and easy to use, but the disadvantage is in its lack of flexibility. While the system can be modified,

it is not ideal for testing software algorithms particularly because it is undesirable to have the system out of operation during prolonged testing. Several AO testbeds in use by the authors use IDL for testing purposes. In this proceeding we present preliminary tests of the FTR for closed-loop operation. These tests were run in our new ‘software’ testbed, which effectively uses the same hardware as the regular system, but controls it through IDL. This software is easy to modify for testing purposes and does not effect the performance of the system for science operations. It should be noted that the IDL system is not ideal for real-time operations and it is not planned to replace the current real-time controller, rather it will be used to test potential modifications to the controller.

3. SYSTEM PERFORMANCE WITHOUT FOURIER RECONSTRUCTION

AO system characterization is an iterative process and this section reviews and expands on the error-budget analysis presented in previous works⁷ for the AO-OCT system. As previously described, typical wavefront residuals for well corrected subjects are less than 100 nm rms, with a large portion of the residual error (approximately 60 nm rms) being low-order errors (less than 2 cycles per aperture) that should be corrected by the system. Figure 2 is the power spectrum of a well corrected subject before correction after bimorph correction, and after MEMS correction.⁷ While each mirror reduces the low-order error it is not reduced to the level of mid-frequency errors. Much of our effort in error budget analysis has been to identify the source of this low-order error.

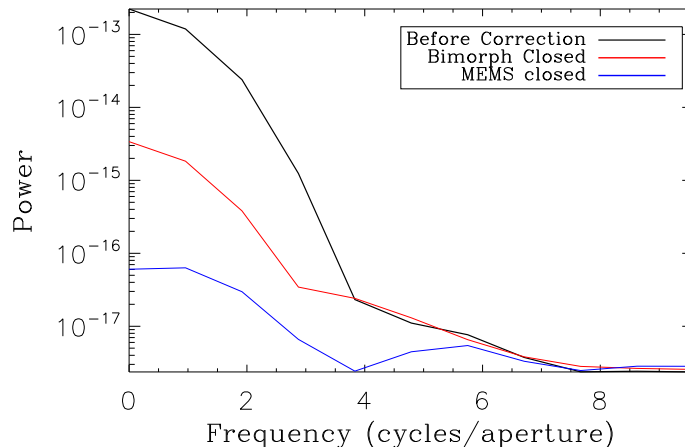


Figure 2. Power spectra of a human subject wavefront, before correction after bimorph correction, and after MEMS correction. Low-order residual errors are reduced in each case but remain a large source of error.

3.1 Measurement Error

Measurement error is a metric of how well the wavefront sensor can measure the wavefront to be corrected. In this proceeding we separate measurement error (errors introduced by centroiding errors in the WFS) from reconstruction error (see Section 3.4). We calculate centroiding error (roughly based on signal to noise) and then we calculate how much wavefront error centroiding errors would introduce to the reconstructed wavefront. Analytical expressions for calculating centroiding error are derived in several papers.¹⁰⁻¹² For the current system the most appropriate equation is the detector limited equation from Nicolle et al.¹⁰ One problem with calculating a single value for measurement error is the large variation in total photons per sub-aperture both across individuals and between subjects. Based on measured parameters of the system, but varying total photons per sub aperture a plot of measurement error can be derived. In Fig. 3 we have plotted centroiding error converted to wavefront error in nm rms based on the FTR used in post processing for the system. Measurement errors resulting from centroiding errors appear to be slightly higher for the VMM reconstruction. The two vertical lines in Fig. 3 indicate the average total photons per sub-aperture for two subjects— one with good correction (subject 13) and one with poor correction (subject 17). There is variation across these individuals as well, as

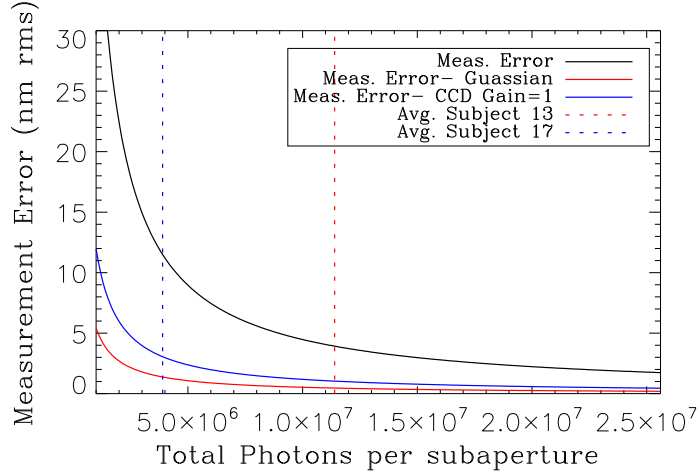


Figure 3. Current Measurement Error is compared to measurement error if the system changed CCD gain settings to 1 or a gaussian-weighted centroider. Measurement error is plotted as a function of total photons per sub-aperture, which varies across the aperture and between subjects. The red vertical dashed line indicates the average total photons per sub-aperture for subject 13, while the blue is for subject 17. Clearly one reason for poor performance of the AO system with some subjects is a decrease in total photons resulting in increased measurement error.

seen in Fig. 4. Clearly one reason for poor performance of the AO system with some subjects is a decrease in

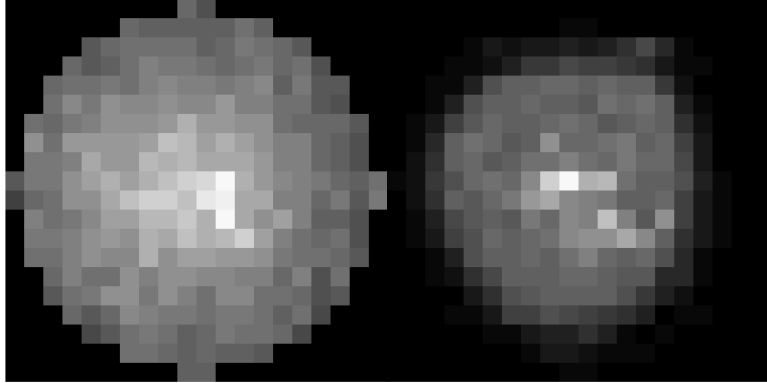


Figure 4. The average total photons per sub-aperture for two subjects. On the left, Subject 13, when the AO System performed well, and on the right Subject 17 for whom the AO system did not perform well. There is variation in the total photons between subjects and even across the aperture for individuals that must be considered when assessing measurement error. The average total photons per sub-aperture for each subject is plotted vertically in Fig. 3.

total photons resulting in increased measurement error as seen in the difference between the total photons of the two subjects presented here. Based on these results we estimate measurement error to be between 6 and 12 nm rms for the FTR and 13 to 26 for the VMM, but caution that at lower light levels measurement errors increase quickly and are likely to be a problem for the robustness of the system.

Understanding the scaling of measurement error with light levels not only helps us understand the robustness of the system to correcting different individuals it also helps us make more informed decisions about AO system upgrades. In Fig. 3 we have also plotted the measurement error expected for the same light levels but with two different system parameters. In one case we have switched to the gaussian-weighted centroider described by Baker et al;¹² In the other we have reduced the read noise of the system by switching the gain of the WFS CCD to 1. In both cases, with the same reflectivity in subjects 13 and 17, we would have reduced measurement error. We have implemented both of these improvement and are currently confirming their performance. In the future, running at higher bandwidths or with increased sub-apertures would reduce the total photons per sub-aperture

and hence increase the measurement error. Examining Fig. 3 suggests that while system performance for ‘good’ subjects would not suffer from even a doubling of the number of sub-apertures, the system would correct fewer subjects well without additional upgrades.

3.2 MEMS Scatter

It was noted in previous characterization work that the MEMS DM has significant backscatter into the WFS when the system is operated in double pass.⁷ BMC suggested that the gold surface of the original MEMS DM was contaminated by outgassing of the glue attaching the MEMS window. To test this BMC provided a MEMS DM without a window and with good surface quality. The backscatter from the two MEMS is compared in Fig. 5. Backscatter in the WFS is measured without a subject or model eye in the system under normal (dark) lighting conditions. Clearly the test device has greatly reduced backscatter compared to the original MEMS. When

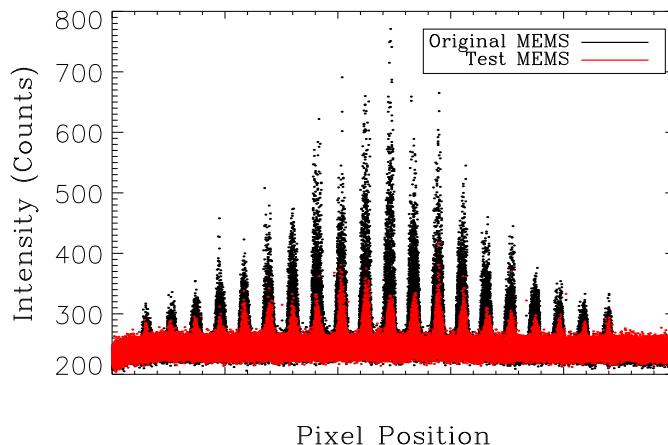


Figure 5. Plot of intensity at every pixel for the WFS for backscattered light in the system. These images are captured when no subject is in the system, and in an ideal system would be only CCD noise. Contamination of the gold surface caused by outgassing of the glue used to attach the MEMS window introduced significant backscatter on the original MEMS device, but a newer test device provided by BMC without the contamination has reduced backscatter. The backscatter of the test device is nearly identical to backscatter from a flat mirror (not shown).

the MEMS mirror is replaced with a flat mirror the backscatter is nearly identical suggesting that remaining backscatter is systematic and not caused exclusively by the MEMS. We plan to replace the MEMS DM in the system in early 2009.

3.3 Bandwidth

The sampling rate of the current AO system is set to 16 Hz. A recent upgrade to the AO control computer should allow the system to run faster, but problems with the interface between the control computer and the AOptix Bimorph mirror are preventing an improved sampling rate. In previous work we used the difference between converged wavefronts to estimate our bandwidth error (within controllable spatial frequencies) to be approximately 33 nm rms.⁷ This is a significant source of error and while most of it is low-frequency it doesn’t completely explain the low-order error seen in the system. The bandwidth can be roughly estimated from the sampling rate to be around 1 Hz, but a more direct measurement is desirable. Currently when AO data are collected for a subject the archive only includes a few frames before the AO loop is turned on, making a comparison of temporal variation with and without AO difficult. We have modified our experimental practices to record more un-corrected data in order to quantify the bandwidth of our system. Not only would this be helpful for an overall error budget it would provide another metric for system variability. Perhaps some poor corrections are caused by changes in the errors introduced by limited bandwidth. Of course another potential limitation to a higher sampling rate is the decreased light level per sub-aperture per timestep. The improvement

in wavefront correction caused by higher bandwidth must be balanced against the increase in wavefront error introduced by measurement errors caused by fewer photons.

Several studies have been conducted to determine the necessary system bandwidth for a vision science AO system.^{13,14} Hofer et al suggest a bandwidth of between 1 and 2 Hz would be optimal, but notes that even low-order errors have temporal variation at up to 5 Hz.¹³ While Santana et al estimate a measurable benefit at even higher bandwidths¹⁴. In both studies the pupil was not dilated, which could introduce more errors. These studies and our data suggest that increased bandwidth is desirable.

Not all bandwidth errors are derived from temporal variations in the eye. The AO sample arm scans the retina and while the double pass configuration should provide a stable pupil plane, the changes in the optical path caused by scanning can introduce wavefront error. With the model eye in place and holding the scanning mirrors at several positions we find that the difference in wavefront can easily be > 50 nm rms. As the scan rate is much faster than the AO sampling rate this is a source of temporal error, although the errors may average out. Alignment of the scan mirrors is critical, but may not be sufficient to controlling this source of error.

3.4 Reconstructor Error

Previously we have investigated reconstructor error and suggested that aliasing within the control matrix might contribute to residual wavefront error in the AO system.⁷ Fundamentally the WFS has 20×20 sub-apertures while the MEMS has only 12×12 . Any reconstructor must down-sample from the WFS to the MEMS. In the VMM no filtering is used and this could lead to aliasing of high-spatial frequency errors that the WFS can measure but the MEMS cannot correct to low spatial frequencies where we expect better AO performance. This should not be confused with aliasing within the WFS, which cannot be measured and must be removed with a spatial filter.¹⁵ In post processing the FTR uses all of the information from the WFS to reconstruct the wavefront and does not down-sample. To quantify the errors introduced by this aliasing we produced a series of wavefronts with varying amounts of error, calculated the WFS slopes from these wavefronts and then reconstructed them using either the FTR or the down-sampling VMM. Any series of wavefronts can be used, but in order to test the effect of higher spatial frequencies the wavefront must contain sufficient amounts of those errors. We attempted to use a series of Zernikes, but with 200 Zernike modes, very little power was produced in the spatial frequencies of interest. Fourier modes are an excellent tool for testing the spatial frequency response of a wavefront reconstructor because they can produce power at all spatial frequencies depending on the sampling of the wavefront. Figure 6 is an example of one individual Fourier mode used for testing.⁷ Individual modes,

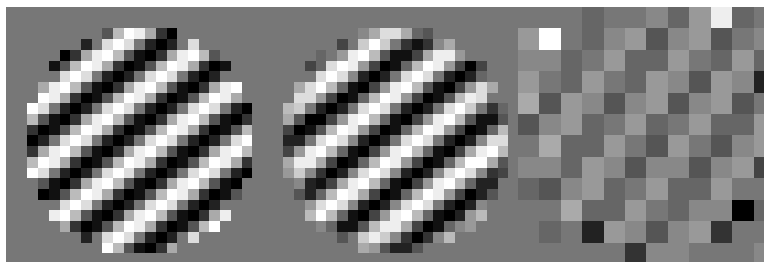


Figure 6. A wavefront with a specific Fourier mode (right) was reconstructed using the Fourier reconstruction (middle) and the VMM reconstruction (left).

while representative of the error, do not help us quantify the size of the reconstructor error. Instead it is useful to sum the low-order error produced from reconstructing each mode using the FTR or the VMM and compare that value to the low-order power in the original signal. In Fig. 7 we plot the rms error summed from 0 to 2 cycles per aperture for the two reconstructed signals and the original signal. The VMM consistently has more low-order error than the input signal. However, if the signal is filtered prior to reconstruction to remove the errors which the WFS can measure but the MEMS cannot correct then additional low-order error is not introduced by the VMM reconstruction (See green line in Fig. 7). For this simulation the amount of high-order error introduced was arbitrary and quite large, which produced high values for the aliased low-order error. Figure 8 is a plot comparing the amount of high-order error introduced in the signal with the amount of low-order error in the reconstruction. Based on this plot we can estimate the 36 nm of out of band error to introduce between 30 and

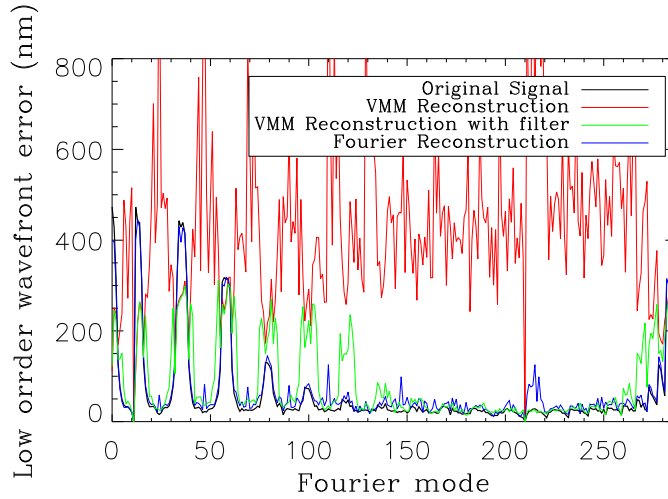


Figure 7. A series of Fourier modes was used to test the VMM and FTR. The rms error from 0 to 2 cycles per aperture is calculated for each mode for the original signal and the two reconstructions. The VMM consistently has more low-order error than the input signal, likely caused by aliasing in the down-sampling from the 20×20 WFS measurement to the 12×12 MEMS array. If the wavefront is filtered to remove high-order errors prior to reconstruction the VMM reconstructor does not introduce additional low-order error.

60 nm rms low-order error, however we caution that this simulation was not ideal as it did not simulate realistic amounts of high-order error and may break down at small values of high order (out of band) error.

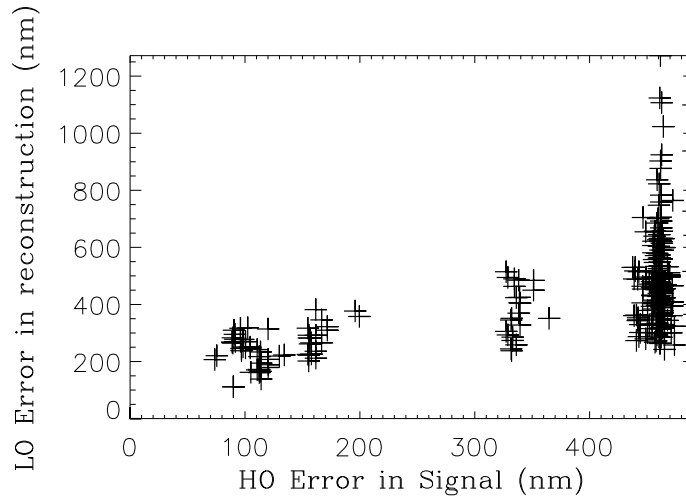


Figure 8. This plot compares higher-order error measured in the input signal to low-order error measured in the reconstructed VMM signal.

There are several ways to correct this type of reconstructor error. In an instrument with matched WFS and deformable mirror this error is not a problem, but when the WFS is over-sampled compared to the DM, filtering is needed to produce the wavefront to be corrected. The FTR uses all of the WFS information to reconstruct and the resulting wavefront can be filtered before it is down-sampled to apply to the deformable mirror or a filter could be applied directly to the control matrix.

3.5 Isoplanatic Error

In a vision AO system, wavefront error is measured from a single point source traveling along a specific angle through the eye. The isoplanatic patch indicates the angle over which the wavefront measured is valid. The size of the isoplanatic patch of the eye has been investigated by several groups and a nice summary of the reported values can be found in Bedggood et al.¹⁶ In general the values range from 1 to 3 degrees. Outside of this region errors can become quite large. However, in the context of the error budget it is important to keep in mind that even within the isoplanatic path anisoplanatism exists. The variation in patch size is in part because of different criteria used for the wavefront error limit within the patch. One of the strictest criteria for isoplanatic angle is the Marechal criteria, which uses a cutoff of $\lambda/14$ for calculating the size of the patch.¹⁶ At our wavelength of approximately 840 nm this indicates that within the isoplanatic path 60 nm rms of wavefront error could be introduced by anisoplanatism. As in most vision systems the AO system is effectively measuring the average wavefront error over the scanned region, which may also affect the frequency content of the isoplanatic errors. Most of the error introduced by anisoplanatism should be measured by the WFS, so if there are unaccounted for errors in our final error budget anisoplanatism is a likely source.

3.6 Calibration Error

A WFS measurement is a relative measurement of wavefront error because it is based on the reference the WFS uses. The calibration error is the error between the relative wavefront measured by the WFS and the actual wavefront error of the system. The current method for obtaining a WFS reference in our system is in Section 2, but an independent means of measuring wavefront error is desirable. A CCD dedicated to measuring the PSF of the system is one way to measure calibration error. Logean et al recently published work indicating the challenges in measuring a real-time double-pass PSF with a human subject,¹⁷ but measurements with a model eye should be much easier and still quantify calibration errors.

4. TESTING FOURIER TRANSFORM RECONSTRUCTION IN CLOSED LOOP

As mentioned in Section 2 we have recently implemented a software ‘testbed’ in IDL to allow testing of new control software without effecting the real-time controller used for normal system operations. This software provides access to the WFS images, and driving of both deformable mirrors without using the real-time controller. After testing the interface between the new software and the hardware, closed-loop control software was implemented. The control software leverages code from astronomical testbeds using the FTR including the Extreme Adaptive Optics (ExAO) Testbed located in the Laboratory for Adaptive Optics at UC Santa Cruz.^{18–20} The focus of the software testbed is to implement and test the FTR, but it could also be used to test techniques for improving the robustness of the system for imaging patients with low reflectivity, dropped WFS spots and/or smaller pupils. FTR has been successfully implemented on several AO testbeds,^{20,21} and is currently used on our system for reconstructing wavefront in post processing, but there are details to implementing this technique in closed loop that must be addressed. In this section we present some of those details, preliminary results and the further work that is needed to improve performance of the FTR. In these initial tests the bimorph mirror was not controlled in closed loop by the FTR system (the geometry of the bimorph makes this type of control more complicated). A flat file from the real time controller for the model eye is applied to the bimorph and then only the MEMS is controlled in closed loop.

4.1 Calibration and Alignment

In the VMM real-time controller, alignment between the WFS and the DMs is effectively measured by the control matrix. Prior to running FTR in closed loop the alignment between the WFS and the MEMS must be measured explicitly. In these tests we applied a voltage to four known actuators placed in a square pattern on the MEMS and used the reconstructed wavefront to calculate the number of pixels per actuator and the vertical and horizontal offsets to align the MEMS with the reconstructed wavefront. Figure 9 is a sample wavefront with the calibration pattern applied (and a reference frame, with no voltage applied, subtracted). The magnification is about 2.2 pixels in the reconstructed wavefront across each MEMS actuator. This over-sampling makes alignment less complicated, but the more advanced techniques used by Poyneer et al^{19,20} on the ExAO testbed, where the

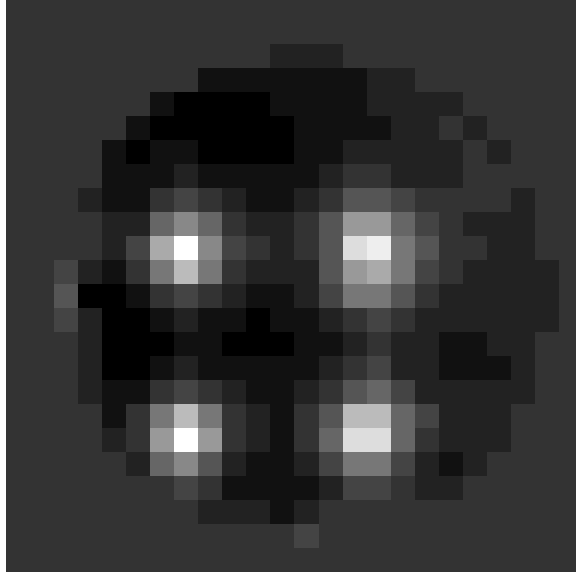


Figure 9. Sample calibration wavefront reconstructed after a four actuator pattern is applied to the MEMS device. A reference wavefront with no voltage applied is subtracted to making centroiding on the 4 actuators more robust.

number of actuators on the MEMS and the sub-apertures of the WFS are matched, may help improve closed-loop performance and will be investigated.

After reconstructing the phase in nm and down-sampling to the MEMS actuators the phase must also be converted to voltage. Ideally the phase to voltage curve would be measured *in situ* at the bias voltage used to run the system, but for these preliminary results we have used the voltage curve provided by BMC for a device with this actuator pitch. Voltage calibration can be measured for every actuator, but typically there is less than 5% variation between actuators and an average of several actuators should be sufficient.¹⁸

4.2 Preliminary Results

The plan for preliminary testing was to not control the bimorph deformable mirror in closed loop but to apply a flat generated from the real-time control software instead, unfortunately this was not successful, leaving the initial phase of the model eye to be corrected quite high. A VMM style controller will be implemented in IDL to flatten the bimorph prior to FTR closed-loop testing. For these tests some of the initial wavefront error was artificially reduced by manipulating the reference to avoid saturating the MEMS. The initial wavefront quality after this adjustment is approximately 250 nm rms. After closing the FTR loop the MEMS reduces the error to about 180 nm rms. The before and after wavefronts are shown in Fig. 10. Clearly some of the error has been removed, but the FTR is not yet working optimally. In Fig. 11 we examine the power spectra of the initial wavefront and two later timesteps. Low-order error is being reduced, particularly around 2 cycles per aperture, which is encouraging, but the overall high level of residual error makes it difficult to draw any conclusions on the effectiveness of the FTR at correcting the low-order error observed with the VMM reconstructor. The large initial wavefront error is difficult for the MEMS to correct and some actuators become saturated preventing improved flattening, but this is unlikely to be the only limitation to improved performance. The alignment between the reconstructed wavefront and the MEMS needed to be adjusted by hand as the horizontal and vertical shift did not seem to be calculated correctly. Improved alignment should improve FTR performance. As suggested in the calibration section the simple alignment using four poked actuators may not be sufficient and will be investigated.

5. ERROR BUDGET SUMMARY

An error budget can be a helpful tool for summarizing AO system characterization, or as a design tool for a future systems because it allows all the constituent errors and their relative sizes to be listed. We have summarized our characterization in Table 1. MEMS precision is the only error not discussed here, but was calculated based

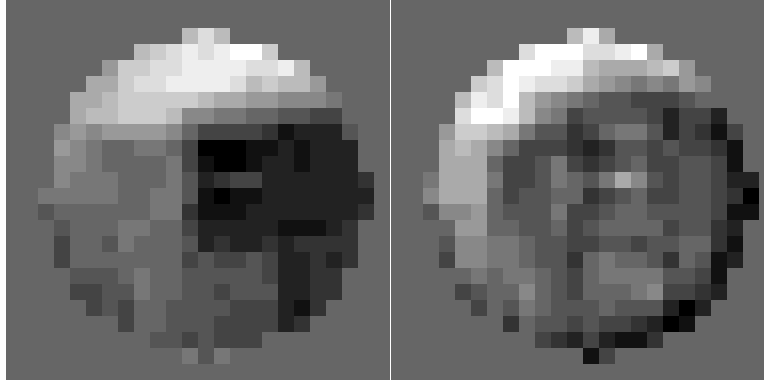


Figure 10. Reconstructed wavefronts before and after the FTR closed loop is run. Wavefront error is reduced from 250 nm rms to 180 nm rms. Clearly some of the error has been removed, but the FTR is not yet working optimally.

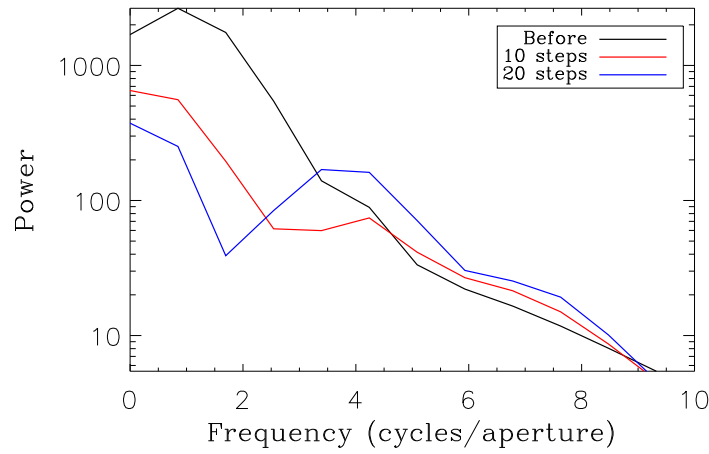


Figure 11. Power spectrum of the initial (uncorrected) wavefront and two later timesteps during FTR closed loop operation. Low-order error is being reduced particularly around 2 cycles per aperture, which is encouraging, but the overall high level of residual error makes it difficult to draw any conclusions about the effectiveness of the FTR at correcting the low-order error observed with the VMM reconstructor.

on the 1% precision of actuator positioning of the MEMS device indicated by BMC.⁷ The largest error remains the uncorrected low-order error that we attribute at least a portion of to aliasing within the control matrix. Improvements to the control system that are underway should reduce this error. Out of band and bandwidth errors are similarly sized, but the relative ease of increasing frame rate of the system compared to increasing the number of actuators suggests that this may be the next area for improvement. An upgrade to the AO system computer should allow the system to run much faster, but interface problems with the Bimorph are an issue.

Error	nm rms
Out of band	36
MEMS precision	12
Measurement	10
Bandwidth	33
Aliasing	30-60
Total Calculated	59-79
Total Measured	95

Table 1. Residual wavefront errors are summarized in an error budget. The largest error remains the uncorrected low-order error that we attribute at least a portion of to aliasing within the control matrix.

The difference between calculated and measured error can be attributed to the remaining errors that are not listed such as MEMS scatter and anisoplanatism. Calibration errors are also not included. The MEMS scatter is not likely to affect performance for subjects with strong reflectivity, but it does effect the robustness of the system particularly for older subjects with poor reflectivity. Variable errors like measurement, and to some extent bandwidth, limit the usefulness of an error budget analysis. While a summary is a useful in its conciseness it will not be useful for improving performance for all subjects, and an AO system should be tailored to the subjects of interest.

6. CONCLUSIONS AND RECOMMENDATIONS FOR IMPROVED SYSTEM PERFORMANCE

We have presented an updated error budget for our AO-OCT system. Correcting aliasing in the control matrix and increasing bandwidth are identified as the top priorities for improving system performance. We also plan to replace the MEMS deformable mirror with a newer version with better surface quality and therefore less scattering. We have demonstrated that the new IDL testbed is interfaced with the hardware and the FTR closed-loop code is operational, but still requires optimization. When the details of the FTR implementation are worked out it can be implemented in the real-time controller. Because of variations in reflected light between subjects measurement error varies and suggests that the single values for constituent errors in the error budget are not sufficient for understanding overall system performance, particularly robustness. We suggest that system robustness would be improved by monitoring and adapting the AO system for changing conditions. For example subjects with poor reflectivity may need slower frame rates to reduce measurement error.

ACKNOWLEDGMENTS

The authors thank Lisa Poyneer for her helpful advice regarding errors in reconstruction and the Fourier Transform Reconstructor. This work performed under the auspices of the U.S. Department of Energy by Lawrence Livermore National Laboratory under Contract DE-AC52-07NA27344. This research was supported by the National Eye Institute (grant EY 014743). This work was supported by funding from the National Science Foundation. The Center for Biophotonics, an NSF Science and Technology Center, is managed by the University of California, Davis, under Cooperative Agreement No. PHY 0120999.

REFERENCES

1. R. Zawadzki, S. Jones, S. Olivier, M. Zhao, B. Bower, J. Izatt, S. Choi, S. Laut, and J. Werner, "Adaptive-optics optical coherence tomography for high-resolution and high-speed 3D retinal in vivo imaging," *Optics Express* **13**(21), pp. 8532–8546, 2005.
2. R. Zawadzki, Y. Zhang, S. Jones, R. Ferguson, S. Choi, B. Cense, J. Evans, D. Chen, D. Miller, S. Olivier, *et al.*, "Ultrahigh-resolution adaptive optics-optical coherence tomography: toward isotropic 3 μm resolution for in vivo retinal imaging," in *Coherence Domain Optical Methods and Optical Coherence Tomography in Biomedicine XI*, J. G. Fujimoto, J. A. Izatt, and V. V. Tuchin, eds., *Proc. SPIE* **6429**, p. 642909, 2007.
3. R. Zawadzki, S. Choi, S. Jones, S. Oliver, and J. Werner, "Adaptive optics-optical coherence tomography: optimizing visualization of microscopic retinal structures in three dimensions," *Journal of the Optical Society of America A* **24**(5), pp. 1373–1383, 2007.
4. R. J. Zawadzki, S. M. Jones, D. C. Chen, S. S. Choi, J. W. Evans, S. S. Olivier, and J. S. Werner, "Retinal imaging with combined adaptive optics, optical coherence tomography and adaptive optics, scanning laser ophthalmoscopy," in *Ophthalmic Technologies XIX*, *Proc. SPIE* **7163** in press.
5. D. A. Horsley, H. Park, and J. S. Laut, Sophie P. and Werner, "Characterization of a bimorph deformable mirror using stroboscopic phase-shifting interferometry," *Sensors and Actuators A: Physical* **134**, pp. 221–230, 2007.
6. T. Bifano, P. Bierden, and J. Perreault, "Micromachined deformable mirrors for dynamic wavefront control," in *Advanced Wavefront Control: Methods, Devices and Applications II*, J. D. Gonglewski, M. T. Grueneisen, and M. K. Giles, eds., *Proc. SPIE* **5553**, pp. 1–16, 2004.

7. J. Evans, R. Zawadzki, S. Jones, S. Okpodu, S. Olivier, and J. Werner, "Performance of a MEMS-based AO-OCT system," in *Proceedings of SPIE*, **6888**, p. 68880G, SPIE, 2008.
8. D. Chen, S. Jones, D. Silva, and S. Olivier, "High-resolution adaptive optics scanning laser ophthalmoscope with dual deformable mirrors," *Journal of the Optical Society of America A* **24**(5), pp. 1305–1312, 2007.
9. L. Poyneer, D. Gavel, and J. Brase, "Fast wave-front reconstruction in large adaptive optics systems with use of the Fourier transform," *Journal of the Optical Society of America A* **19**(10), pp. 2100–2111, 2002.
10. M. Nicolle, T. Fusco, G. Rousset, and V. Michau, "Improvement of Shack-Hartmann wave-front sensor measurement for extreme adaptive optics," *Optics Letters* **29**(23), pp. 2743–2745, 2004.
11. P. Prieto, F. Vargas-Martín, S. Goelz, and P. Artal, "Analysis of the performance of the Hartmann-Shack sensor in the human eye," *Journal of the Optical Society of America A* **17**(8), pp. 1388–1398, 2000.
12. K. Baker and M. Moallem, "Iteratively weighted centroiding for Shack-Hartmann wave-front sensors," *Optics Express* **15**(8), pp. 5147–5159, 2007.
13. H. Hofer, P. Artal, B. Singer, J. Aragón, and D. Williams, "Dynamics of the eyes wave aberration," *Journal of the Optical Society of America A* **18**(3), pp. 497–506, 2001.
14. L. Diaz-Santana, C. Torti, I. Munro, P. Gasson, and C. Dainty, "Benefit of higher closed-loop bandwidths in ocular adaptive optics," *Optics Express* **11**(20), pp. 2597–2605, 2003.
15. L. A. Poyneer, B. Bauman, B. A. Macintosh, D. Dillon, and S. Severson, "Spatially filtered wave-front sensor for high-order adaptive optics," *Opt. Lett.* **31**, pp. 293–295, 2006.
16. P. Bedggood, M. Daaboul, R. Ashman, G. Smith, and A. Metha, "Characteristics of the human isoplanatic patch and implications for adaptive optics retinal imaging," *Journal of Biomedical Optics* **13**, p. 024008, 2008.
17. E. Logean, E. Dalimier, and C. Dainty, "Measured double-pass intensity point-spread function after adaptive optics correction of ocular aberrations," *Optics Express* **16**(22), pp. 17348–17357, 2008.
18. J. W. Evans, B. A. Macintosh, L. Poyneer, K. Morzinski, S. Severson, D. Dillon, D. Gavel, and L. Reza, "Demonstrating sub-nm closed loop MEMS flattening," *Optics Express* **14**, pp. 5558–5570, 2006.
19. L. A. Poyneer and B. Macintosh, "Experimental demonstration of phase correction with a 32 x 32 microelectricalmechanical systems mirror and a spatially filtered wavefront sensor," *J. Opt. Soc. Am. A* **21**, pp. 810–819, 2004.
20. L. Poyneer, D. Dillon, S. Thomas, and B. Macintosh, "Laboratory demonstration of accurate and efficient nanometer-level wavefront control for extreme adaptive optics," *Applied Optics* **47**(9), pp. 1317–1326, 2008.
21. L. Poyneer, M. Troy, B. Macintosh, and D. Gavel, "Experimental validation of Fourier-transform wave-front reconstruction at the Palomar Observatory," *Optics Letters* **28**(10), pp. 798–800, 2003.